Chen et al. *NPG Asia Materials* (2023) 15:64
https://doi.org/10.1038/s41427-023-00507-7

NPG Asia Materials

ARTICLE Open Access

Light-enhanced osmotic energy generation with an aramid nanofiber membrane

Cheng Chen[1,2], Yunxiao Lin[3], Weiwei Lei[2], Guoliang Yang[2], Yuchen Liu[2], Mao Xu[1], Xinhao Li[3] and Dan Liu[2]

Abstract

Osmotic energy generation with reverse electrodialysis through membranes provides a worldwide free energy resource. Photo-driven proton transport in photosynthesis supplies basal energy for plants and living organisms on the planet. Here, we utilized aramid nanofiber (ANF) semiconductor-based membranes to enable light-driven proton transport for osmotic energy generation. Under unilateral illumination, the light-driven proton transport system converted light energy into electrical energy and showed wavelength- and intensity-dependent transmembrane potentials and currents. Interestingly, the synergistic effects of simultaneous illumination and pressure provided a five-fold increase in the voltage and a three-fold increase in the current relative to pressure alone. Density functional theory calculations and spectroscopic measurements demonstrated that the ANF and photoinduced electrons enabled proton transport during illumination and generated a transmembrane potential and current. The light-driven proton transport system supports the development of devices with flexible and stable ANF membranes.

Introduction

Osmotic energy is a sustainable, lavish, and competitive source of clean energy, and it has drawn tremendous interest based on the convergence of physical, chemical, engineering, and materials sciences[1,2]. Theoretically, the intriguing osmotic energy of 2.3 MJ per cubic meter of water is generated by the chemical potential difference between seawater and lake water[2]. To extract this chemical potential energy, conventional positively and negatively charged polymer membranes are packed in stacks to collect the electricity directly resulting from the reverse electrodialysis (RED) process[3,4]. Although many studies have been focused on membrane design[5–7], the conversion of sustainable energy from osmotic energy remains an open field.

Photosynthesis by chlorophyll and bacteriorhodopsin (bR) systems supports and nourishes the living organisms on earth[8]. When the chlorophyll system is illuminated with sunlight, charge separation via electron transfer (electron transport) between pheophytin and quinone forms a proton gradient and generates electric energy from solar radiation[9]. Under solar light, the energy level of the lowest unoccupied molecular orbital (LUMO) and the highest occupied molecular orbital (HOMO) are responsible for the potential, and the photoexcited holes provide oxidation sites, and electrons provide the reduction sites[10–13]. Thus, in using sunlight to promote photochemical reactions or produce solar fuels, we must design active membranes to capture photons at the reactive sites and transfer the excitation energy. Based on the chlorophyll system, artificial photocatalysts have been explored for solar fuel production[10–12,14,15]. In the bR system, the proton gradients (electrochemical gradients) in biological systems drive metabolic processes by converting the electric energy into chemical energy[16,17]. As in the bR process, polymeric membranes have been developed to study light-produced electrical currents and voltages with H^+ taken up and released during solar irradiation[16]. The

Correspondence: Cheng Chen (chc@ahau.edu.cn) or
Weiwei Lei (weiwei.lei@deakin.edu.au) or Dan Liu (dan.liu@deakin.edu.au)
[1]School of Resources and Environment, Anhui Agricultural University, 130 Changjiang West Road, Hefei 230036 Anhui, China
[2]Institute for Frontier Materials, Deakin University, Locked Bag 2000, Geelong, VIC 3220, Australia
Full list of author information is available at the end of the article
These authors contributed equally: Cheng Chen, Yunxiao Lin

protons collected at the solution interface with the Nafion ion-exchange membrane facilitate sunlight-driven ion transport[18]. Hence, solar-triggered electrochemical gradients and photoelectric generation are connected[19]. Significant advances have enhanced proton transport conversion to electric energy with solar energy; however, photon-to-gradient conversion is still in its infancy compared to biological light-driven ion transport systems, which directly convert light energy into chemical energy[20]. Thus, light-driven proton transport would have numerous promising applications, but the encouraging and challenging work remains to be done.

Recent works showed that light could stimulate a membrane and enhance osmotic energy harvesting, such as with the photochromic compounds, C_3N_4, graphene, and MoS_2[7,16,21,22]. Solar energy can be converted to electrical energy[23,24]. Aramid nanofibers (ANFs), which are produced from PPTA (poly(paraphenylene terephthalamide)), are state-of-the-art nanoscale composites with excellent mechanical breaking strengths and numerous surface groups[25]. ANFs have been widely studied for use in dendrite-suppressing ion conductors, supercapacitors, nanofiltration membranes, lithium-ion batteries, and electrical heaters[26–30]. We recently found that the use of aramid as a proton membrane enabling high-performance osmotic energy harvesting, similar to graphene, boron nitride, and atomically thin micas[31,32]. The proton gradient in the aramid membrane is a versatile energy source that drives endothermic reactions such as ATP synthesis[33]. Therefore, the aramid membrane exhibits great potential for photoelectric energy conversion.

Herein, we first used DFT calculations to show that the electronic structures of ANFs have the photoactivity required to convert light into electricity. Then, ANF membranes featuring flexible, substantial, and desirable thicknesses were prepared via filtration of different amounts of aramid nanofiber (ANF) dispersed in deionized water (DI). The ANF membrane showed an impressive breaking strength of 90 MPa. More importantly, when illuminated with simulated sunlight, the ANF membrane exhibited a light response current and voltage, depending on the wavelength and intensity of the light. When the ANF membrane device was treated with light and pressure simultaneously, the potential and current increased accordingly. Spectral measurements and DFT calculations were used to study the mechanism for proton transport. We demonstrated that the ANF-based membrane can be used for photoelectric conversion devices.

Results and discussion

DFT calculation of the ANF membrane

We carried out density functional theory (DFT) calculations[34,35] to understand the electronic structure of the ANFs. As shown in Fig. 1A, the ANFs showed an indirect band gap of 2.51 eV, based on the calculated band structures resulting from the k-points in the first Brillouin zone with an ideal infinite model along the high symmetry line. Impressively, the calculated band gap of the ANFs was consistent with the experimental value (2.61 eV) (Fig. S1). The partial density of states (PDOS), as well as the wave functions for both the lowest unoccupied molecular orbital (LUMO) and highest occupied molecular orbital (HOMO), were analyzed, as shown in Fig. 1B–D. It is clear that the HOMO and the LUMO were derived from the 2*p* orbitals providing good π-delocalization throughout the polymer chains. Then, we measured the photocurrents of film electrodes on an FTO substrate to assess the photoelectric responses of the ANF membrane in 0.5 M Na_2SO_4 with a pH of 6.8. As shown in Fig. S2, the current-potential (I–V) profile of the ANF photoelectrode showed a remarkable photoresponse with periodic light on/off shifts. Extraordinarily, the anodic photocurrent of the ANFs was ca. 0.76 $\mu A cm^{-2}$ at 1.8 V vs. RHE with a bias voltage above 0.4 V vs. RHE. Considering the calculated results and the photoelectrochemical performance of the ANFs, we explored their use in photoelectric energy conversion because the band gap could produce a strong photocurrent. In addition, the energy required for the conversion of H_2O to H_2 was found to slightly exceed the ECB of the ANFs, so water splitting is energetically infeasible (Fig. S3). Therefore, the band structure of the ANFs allow organized transfer of photogenerated electrons and holes in the form of protons and make the ANFs promising candidates for light-driven proton transport (Fig. 1E).

Synthesis and characterization of the ANF membranes

The preparations of the ANF membranes and the characterization data are shown in Fig. 2. The ANF solution was first prepared via the protocol reported by Yang et al. [36]. Then, excess DI water was added to the DMSO-dispersed ANF dispersion, and the dispersed ANF solutions gelled and aggregated quickly. After magnetic stirring for two weeks in water with KOH (0.1 $mol \cdot L^{-1}$), the ANF solution was well dispersed in the DI water (Figs. 2A, S4, S5). The ANF dispersion was then placed onto a nylon membrane substrate to produce the ANF membrane with vacuum filtration (Fig. S6). The thicknesses of the ANF membranes were easily adjusted by filtrating various amounts of the AFN dispersion. After drying at 60 °C for half an hour, the ANF membrane was peeled off from the nylon membrane substrate with water based on the Rehbinder effect. The resulting ANF membrane was approximately ten μm thick, as shown by a cross-sectional SEM image (Fig. 1C). In addition, the SEM image shows that the ANF membrane maintained the nanofiber structure in the layered structure membrane. Notably, the

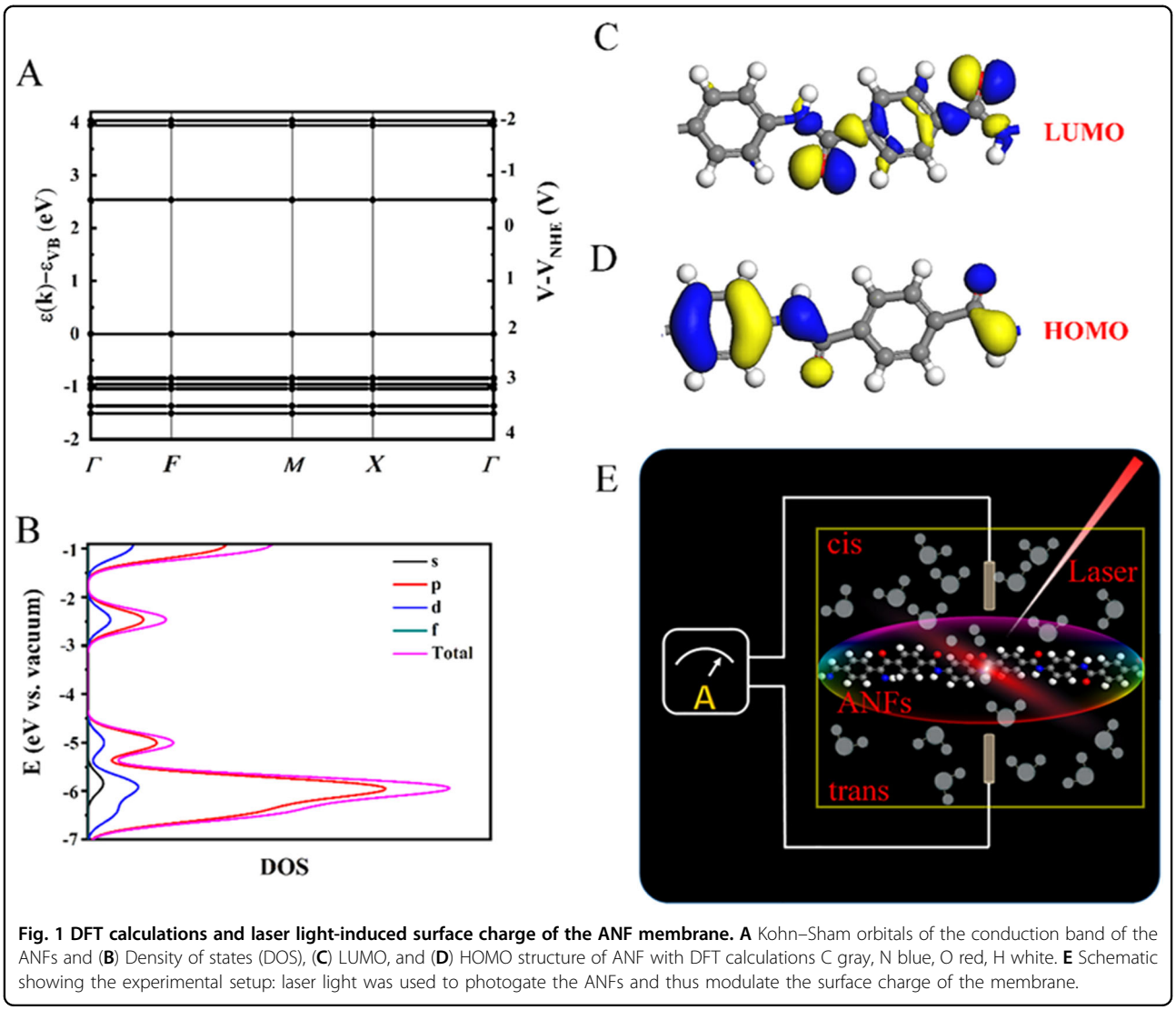

Fig. 1 DFT calculations and laser light-induced surface charge of the ANF membrane. A Kohn–Sham orbitals of the conduction band of the ANFs and (**B**) Density of states (DOS), (**C**) LUMO, and (**D**) HOMO structure of ANF with DFT calculations C gray, N blue, O red, H white. **E** Schematic showing the experimental setup: laser light was used to photogate the ANFs and thus modulate the surface charge of the membrane.

one-dimensional (1D) nanoscale building blocks of the membranes produced structural nanochannels around the ANFs and interspaces in the ANF building blocks to support proton transport.

The basic physical and chemical structural properties of the ANF membranes were characterized with X-ray diffraction (XRD), FTIR-ATR spectroscopy, and Raman spectroscopy. Figure 2B shows the XRD pattern for the ANF membrane. The XRD pattern showed broad peaks at ~20°, ~23°, and ~29°, which were attributed to the (110), (200), and (004) planes of the aramid, respectively[37,38]. After one hour of illumination with a laser (405 nm) in HCl (1 mol·L^{-1}), the ANF membrane exhibited XRD peaks similar to those of the fresh ANF membrane. Raman spectroscopy showed that the fresh and treated ANF membranes exhibited spectra identical to those previously reported (Fig. 2C)[36]. The ANF membrane showed characteristic peaks for C = C stretching (1181, 1277, 1514, and 1610 cm^{-1}), C − H in-plane bending at 1327 cm^{-1}, N − H bending/C − N stretching at 1569 cm^{-1}, and C = O stretching at 1648 cm^{-1} [36]. The FTIR-ATR spectra were used to identify the surface functional groups of the ANF membrane (Fig. 2D). The appearance of the N–H stretching vibrations (a broad peak at 3300 cm^{-1}) and the carboxyl stretching vibration (C = O, 1650 cm^{-1}) indicated amides[37]. The band at 1650 cm^{-1} for C = O species forming intrananofiber hydrogen bonds remained stable even when illuminated with the laser. The strength of the ANF membrane (2.5 mm × 12 mm) was tested with an Instron 5960 Series Tensile Tester (Instron Corporation), which showed a break strength and Young's modulus of 90 MPa and 2.38 GPa (Fig. S7), respectively, which were comparable to those of natural nacre and reported nanocomposite membranes[39–43]. The strong hydrogen bonds of the aramid nanofibers accounted for the high mechanical

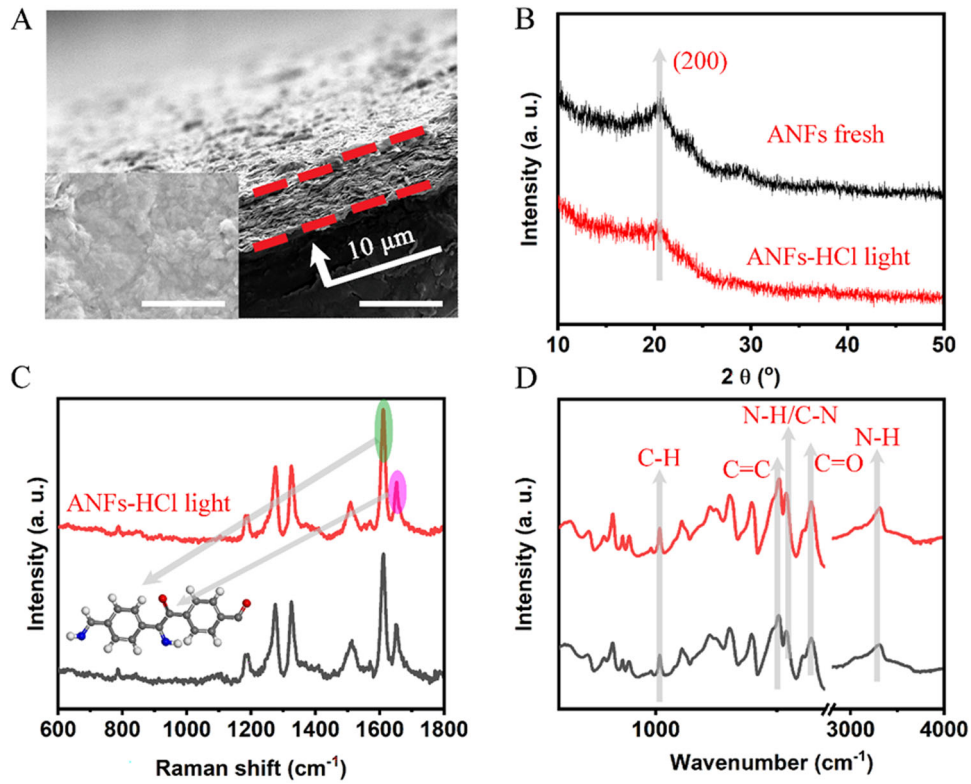

Fig. 2 Preparation of the ANF membrane and structural characterization. A Cross-sectional and surface SEM images of an ANF membrane. The left inset is the top-view SEM image of the ANF membrane. **B** XRD patterns of the fresh and illuminated ANF membranes in HCl. **C** Raman spectra of the fresh and illuminated ANF membranes in HCl. **D** FTIR-ATR spectra of the fresh and illuminated ANF membranes in HCl.

strength of the ANF membrane[36]. Therefore, the XRD, Raman, FTIR-ATR, and tensile strength results indicated the structural and chemical stability of the ANF membrane during laser illumination, which confirmed the potential of using the ANF membrane under solar illumination.

Solar energy conversion to osmotic energy with the ANF membrane

Figure 3A, B show the current–voltage (I–V) characteristics of the ANF membrane studied in the dark and under replicated 100 mW·cm^{-2} solar illumination (with a laser dot measuring 405 nm)[5]. When tested with DI water, the I–V response of the ANF membrane changed distinctly during illumination relative to the response seen in the dark. Indeed, in the dark environment, the I–V characteristics were consistent with the zero-current voltage of 0 V. Impressively, the I–V characteristics showed that the slope of the I increased during illumination with the zero-current voltage at 16 mV. In addition, the increased current generated by illumination was indicated by the higher bias voltage compared with that of the dark case. Then, the slope of the curve was used to determine the conductance of the ANF membrane with and without solar illumination[44]. This is a direct way to prove that solar illumination increased the conductance of the ANF membrane, indicating a photoelectric effect in DI water.

The proton transport performance was measured in a customized H-cell setup without a bias voltage. Twelve milliliters of DI water was added to the two reservoirs. Figure 3C, D show the typical photodriven current and voltage of the ANF membrane measured during laser illumination with purple light (405 nm) at 100 mW·cm^{-2}. The control experiment without light showed no current or voltage due to the balance between the two reservoirs. With the illumination of the ANF-10 membrane, the solar-induced current and voltage increased and decreased periodically as the light was switched on and off (Fig. 3C, D). Typically, with the light on, the voltage increased from zero to 10 mV in 60 s, while the current increased to 1 nA in 60 s. Then, with the light off, the voltage decreased from 10 mV to 2 mV in 60 s, and the current decreased from 1 nA to 0.2 nA in 60 s. Five voltage and current cycles with light on/off switching showed the stable photoresponse of the ANF membrane.

The power density and wavelength effects were investigated to understand the proton transport “power”. With

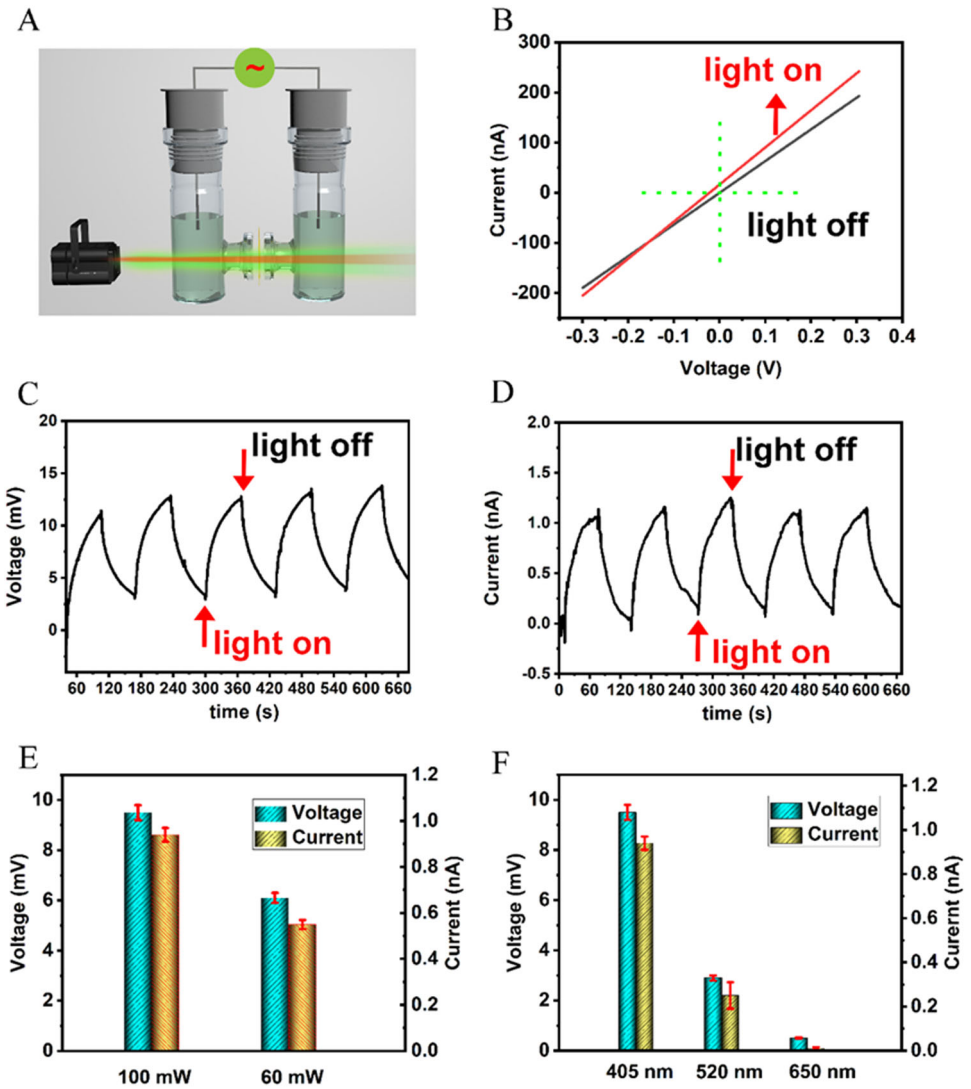

Fig. 3 Use of the ANF-10 membrane in light-driven proton transport. A Schematic of the H-cell setup. **B** I–V curves for DI water with the two reservoirs connected by the ANF membrane with and without illumination. **C** Photo-driven voltage by the ANF membrane. **D** Photo-driven current by the ANF membrane. **E** Photo-driven proton transport versus light intensity. **F** Photo-driven proton transport versus the wavelength of the light.

a constant wavelength of 405 nm, the light-induced current and voltage decreased as the illumination density was decreased (Fig. 3E). Compared with 100 mW·cm^{-2} light illuminating the ANF membrane, 60 mW·cm^{-2} illumination produced a 30% lower current and voltage. This implied that a higher solar density would improve the electron energy conversion efficiency. To study the relationship between the wavelength and osmotic energy conversion, we used different monochromatic lights with the same power density (100 mW·cm^{-2}) to irradiate the ANF membrane (Fig. 3F). The ANF membrane showed a high voltage and current with purple light (405 nm) and lower voltages and currents with green light at 520 nm and red light at 650 nm. These results were consistent with the light absorbed by the ANF membrane and confirmed that the solar energy is converted into electron energy by the ANF membrane in DI water.

Optimizing the conversion of solar energy to osmotic energy with the ANF membrane

Additional measurements showed that the current and voltage generated were dependent on the pH of the solution[12]. Subsequent measurements were performed with the same solar illumination conditions (405 nm, 100 mW·cm^{-2})[16]. As the pH of electrolyte was reduced from 6 to 4, the photodriven voltage decreased rapidly from the highest solar-induced voltage of 13 mV to nearly 0 mV (Fig. 4A). Similarly, the current gradually declined from 1 nA to zero when decreasing the pH from 6 to 4 (Fig. 4B). Then, as the pH was reduced from 3 to 1, the

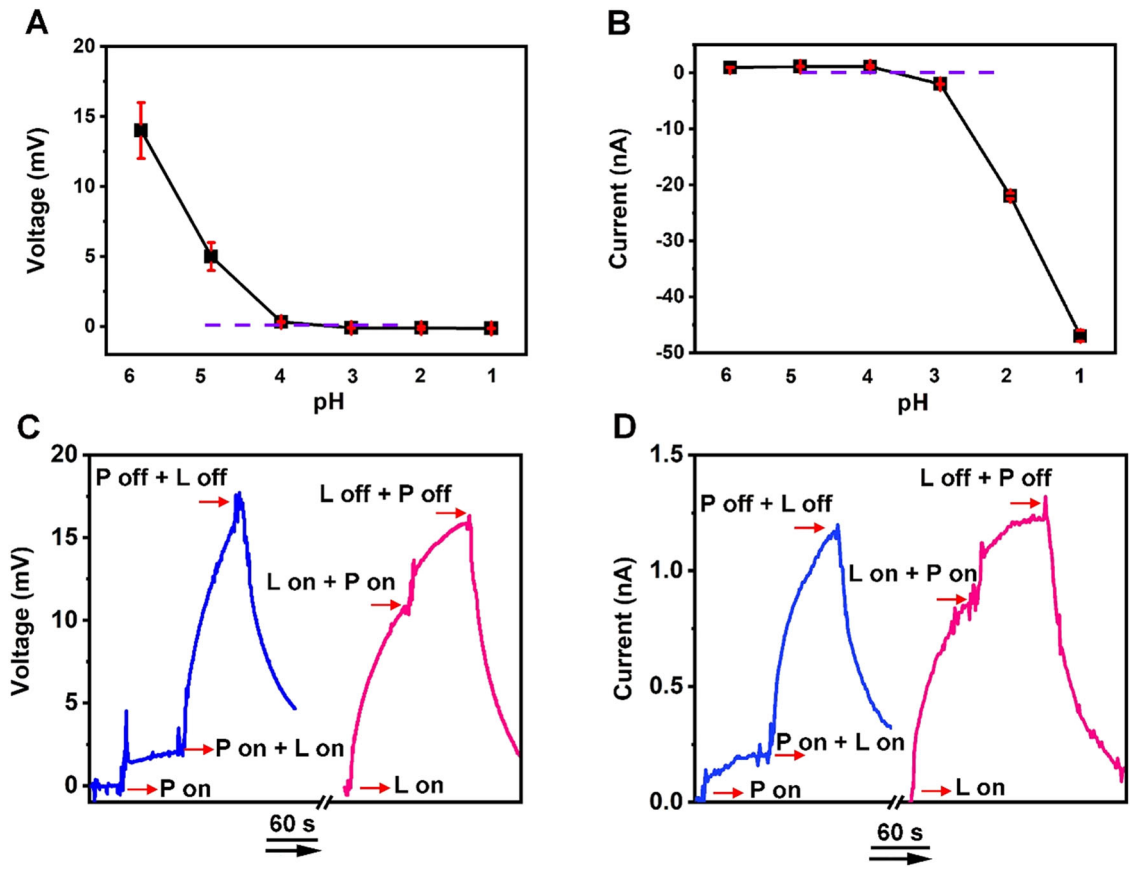

Fig. 4 Optimization of the photodriven current and voltage production. pH effects on the driving voltage (**A**) and current (**B**). Synergistic effects of pressure and illumination on the ANF-10 to improve the voltage (**C**) and current (**D**). P was a 5 kPa nitrogen pressure, and L is 405 nm light at 100 mW·cm^{-2}.

photodriven voltage showed a slow approach to 0 mV. However, the photodriven current increased rapidly as the pH was decreased from 3 to 1. The most significant solar-induced current was -45 nA, which resulted from illumination at 405 nm with the laser.

Furthermore, within a pH range of 4 to 3, the solar-induced current and voltage changed the direction of electron transport. Hence, the ANF membrane showed the potential for generating alternating current and voltage with pH changes. Acidic DI water could have protonated the ANF membrane, which generated a positive charge on the membrane. The charged ANF membrane determined the photodriven electron direction, resulting in positive and negative currents and voltages. Moreover, at high pH, the negatively charged ANF membrane showed higher proton selectivity and a higher photodriven voltage. In the low pH range, the proton concentration in the DI water increased the photocurrent.

The synergistic effect of solar energy and hydraulic pressure on energy conversion was also studied. Taking the DI water as an example, a nitrogen pressure of 5 kPa was applied on one side of the ANF membrane for 60 s, and the membrane converted the hydraulic pressure into a streaming proton voltage. Then, with the pressure maintained, a dot of light was shone on the membrane side under pressure. A higher voltage was generated with simultaneous pressure and irradiation. Similarly, with the illumination of the membrane, the pressure on the membrane generated a comparable voltage of approximately 17 mV. The pressure and light also converted the solar and hydraulic pressure to current (Fig. 4C, D). With the light and pressure on the membrane, a current of nearly 1.2 nA was generated. Then, the pressure and light were applied from opposite directions, which showed a similar synergistic effect in which solar energy and hydraulic pressure generated electron transport. While two lights were shone on the H-cell device from opposite directions and the pressure was on, the currents were offset (Fig. S8). Although the photodriven voltage and current were insufficient for practical power devices, they could be integrated into other membrane devices to harvest energy with proton transport. The ANF

membrane has the potential to convert solar energy and hydraulic pressure into electrical energy, as seen with reported fragile membranes[7,16,21,22].

Conclusion

In summary, we developed an aramid nanofiber membrane enabling proton transport for photoelectron energy conversion. Spectroscopic measurements and DFT calculations verified that the aramid membrane had suitable HOMO and LUMO energies and could convert photoenergy into electric energy. Under illumination in DI water, the photoinduced ion transport system produced a voltage and current dependent on the light intensity and wavelength. Solar energy and hydraulic pressure energy were combined to increase energy harvesting. The theoretical simulations and experimental results showed that the photogenerated charges and holes were transported across the ANF membrane. This work provides a strategy for using abundant and sustainable solar energy in harvesting osmotic energy.

Material and methods

Materials

Bulk Kevlar 69 with a right twist was used as the raw material and was purchased from Thread Exchange. Dimethyl sulfoxide (DMSO) and potassium hydroxide (KOH) were acquired from the Sigma-Aldrich. All chemicals were used as purchased.

Aramid membrane preparation

One gram of bulk aramid was first cut into 1–3 cm pieces and then mixed with DMSO (500 mL) and KOH (1.5 g) according to Yang's method[36]. Dissociation of the bulk aramid took two weeks, and water segregation was necessary. Then, 1000 mL of DI water was added to 100 mL of the aramid dispersion to make the nanofiber gel. After filtration of the extra DMSO, the aramid nanofibers were redispersed and stored in a 100 mL KOH (0.1 mol L^{-1}) solution. Aramid membranes with different thicknesses were obtained via filtration of various amounts of aramid nanofiber dispersions on a nylon membrane. Then, 1000 mL DI water was used to wash out the excess KOH. The prepared ANF membranes were easily peeled off with 2 mL of DI water after drying at 60 °C for one hour in an oven.

DFT calculations

All theoretical calculations were performed with density functional theory (DFT) and the Materials Studio 8.0 in the DMol3 program. The electronic exchange-correlation energy was provided by the generalized gradient approximation (GGA) method with the spin-polarized Perdew-Burke-Ernzerhof (PBE) function[34]. Valence orbitals were expressed with the double numerical plus polarization (DNP) basis[35].

Mechanical measurements

The mechanical measurements of the ANF membranes (2.5 mm × 12 cm) were performed with an Instron 5960 Series Tensile Tester (Instron Corporation). For each test, the stress–strain profiles were determined at a rate of 10 mm min^{-1} with an ~5 N range load cell. Three parallel tests were performed for each sample. The stress (σ) of the ANF membranes was calculated with the following formula:

$$\sigma = F/(a \times b) \quad (1)$$

where F is the loading force (N), a is the width (2.5×10^{-4} m), and b is the thickness of the membrane (10×10^{-6} m). Hence, the maximum loading force refers to the breaking stress. The strain (ε) was calculated as follows:

$$\varepsilon = \Delta L/L \times 100\% \quad (2)$$

where ΔL is the change in membrane length, and L is the original membrane length (12×10^{-4} m).

Photoelectronic energy conversion

photoelectronic energy conversion with the aramid membrane was investigated with and without illumination by recording the short ionic current and open circuit voltage. An aramid membrane with an effective area of 3.14 mm^2 was mounted between two compartments of a homemade H cell. The H cell was filled with 12 mL of electrolyte solution with the same concentration for each test. A Keithley 6517B ammeter was used to collect the current and voltage signals with Ag/AgCl electrodes. Please note that the light should not illuminate the Ag/AgCl electrodes. The ANF-10 membrane was used for additional investigations because of the intriguing solar-induced current and voltage compared to those of the thick and thin ANF membranes.

Synergistic effect of photoelectron energy and pressure-driven streaming

The ANF membrane was mounted in a sealed H cell in a typical experiment. Then, nitrogen gas with the desired pressure was applied to the selected compartment and controlled with an outside valve. The synergistic effect was determined with pressure and light on/off cycles. A Keithley 6517B ammeter connected to the two Ag/AgCl electrodes was used to measure the current and voltage responses. The collected current flowing out from the pressurized side was defined as positive.

Characterization

XRD patterns were collected with a Bruker D8 Advance diffractometer with Cu Kα radiation (λ = 1.5406 Å). The FTIR-ATR spectra were obtained with a Nicolet 7199 FTIR spectrometer. Raman spectroscopic measurements were performed with a Renishaw Raman spectrometer (514 nm). The UV–Vis spectra were recorded with a Cary

500 Scan Spectrophotometer (Varian, USA). Here, $BaSO_4$ was utilized as a reflectance standard for ultraviolet–visible diffuse reflectance spectroscopy. A Zeiss Supra 55 VP system was used to investigate the sample morphologies, and each sample was coated with 5 nm of carbon to reduce the charge effect. Photoelectrochemical measurements were conducted with a BAS Epsilon Electrochemical System in a three-electrode cell, where a Ag/AgCl electrode (3 M KCl) was used as the reference electrode, and a Pt plate was used as the counter electrode. Each sample slurry (5 mg ml^{-1} in DMF) was spread on indium-tin oxide to construct the working electrode. After air drying, the working electrode (ANFs on ITO) was put into a 0.2 M Na_2SO_4 aqueous solution (pH = 6.8).

Acknowledgements
This work was financially supported by the Australian Research Council Discovery Programs (DP190103290, DP220103416) and Australian Research Council Future Fellowships (FT200100730, FT210100804). C.C. thanks the National Natural Science Foundation of China (Grant No. 42207521), the Natural Science Foundation for the Higher Education Institutions of Anhui Province of China (KJ2020ZD10), and the Anhui Provincial Returnees Innovation and Entrepreneurship Key Support Program (2022LCX003).

Author details
[1]School of Resources and Environment, Anhui Agricultural University, 130 Changjiang West Road, Hefei 230036 Anhui, China. [2]Institute for Frontier Materials, Deakin University, Locked Bag 2000, Geelong, VIC 3220, Australia. [3]School of Chemistry and Chemical Engineering, Shanghai Jiao Tong University, Shanghai, China

Author contributions
D.L., W.L. and C.C. conceived the project. C.C., D.L., X.L. and W.L. designed the experiments. C.C. and D.L. carried out the material syntheses. Y.L. and X.L. performed the DFT calculations. C.C., G.Y., Y.L. and M.X. performed the osmotic energy harvesting measurements. C.C., Y.L., D.L., X.L. and W.L. wrote the manuscript. All authors discussed the results and commented on the manuscript.

Competing interests
The authors declare no competing interests.

Supplementary information The online version contains supplementary material available at https://doi.org/10.1038/s41427-023-00507-7.

Received: 23 November 2022 Revised: 14 September 2023 Accepted: 11 October 2023.
Published online: 8 December 2023

References

1. Siria, A., Bocquet, M.-L. & Bocquet, L. New avenues for the large-scale harvesting of osmotic energy. *Nat. Rev. Chem.* **1**, 1–10 (2017).
2. Zhang, Z., Wen, L. & Jiang, L. Nanofluidics for osmotic energy conversion. *Nat. Rev. Mater.* **6**, 622–639 (2021).
3. Cui, Y., Liu, X.-Y. & Chung, T.-S. Enhanced osmotic energy generation from salinity gradients by modifying thin film composite membranes. *Chem. Eng. J.* **242**, 195–203 (2014).
4. Tong, X., Liu, S., Crittenden, J. & Chen, Y. Nanofluidic membranes to address the challenges of salinity gradient power harvesting. *ACS Nano* **15**, 5838–5860 (2021).
5. Xiao, K. et al. Light-driven directional ion transport for enhanced osmotic energy harvesting. *Natl Sci. Rev.* **8**, nwaa231 (2021).
6. Yang, G. et al. Simultaneous electrokinetic energy conversion and organic molecular sieving by two-dimensional confined nanochannels. *Chem. Eng. J.* **446**, 136870 (2022).
7. Xiao, K. et al. Artificial light-driven ion pump for photoelectric energy conversion. *Nat. Commun.* **10**, 1–7 (2019).
8. El-Sayed, M. On the molecular mechanisms of the solar to electric energy conversion by the other photosynthetic system in nature, bacteriorhodopsin. *Acc. Chem. Res.* **25**, 279–286 (1992).
9. Scholes, G. D., Fleming, G. R., Olaya-Castro, A. & Van Grondelle, R. Lessons from nature about solar light harvesting. *Nat. Chem.* **3**, 763–774 (2011).
10. Wang, X. et al. A metal-free polymeric photocatalyst for hydrogen production from water under visible light. *Nat. Mater.* **8**, 76–80 (2009).
11. Ji, D. et al. Band-like transport in small-molecule thin films toward high mobility and ultrahigh detectivity phototransistor arrays. *Nat. Commun.* **10**, 1–8 (2019).
12. Bi, S. et al. Two-dimensional semiconducting covalent organic frameworks via condensation at arylmethyl carbon atoms. *Nat. Commun.* **10**, 1–10 (2019).
13. Wang, R. et al. Nanoscale 2D g-C_3N_4 decorating 3D hierarchical architecture LDH for artificial photosynthesis and mechanism insight. *Chem. Eng. J.* **448**, 137338 (2022).
14. Fujishima, A. & Honda, K. Electrochemical photolysis of water at a semiconductor electrode. *Nature* **238**, 37–38 (1972).
15. Jin, E. et al. Two-dimensional sp2 carbon–conjugated covalent organic frameworks. *Science* **357**, 673–676 (2017).
16. Xie, X., Crespo, G. A., Mistlberger, G. & Bakker, E. Photocurrent generation based on a light-driven proton pump in an artificial liquid membrane. *Nat. Chem.* **6**, 202–207 (2014).
17. Gadsby, D. C. Ion channels versus ion pumps: the principal difference, in principle. *Nat. Rev. Mol. Cell Biol.* **10**, 344–352 (2009).
18. White, W., Sanborn, C. D., Reiter, R. S., Fabian, D. M. & Ardo, S. Observation of photovoltaic action from photoacid-modified nafion due to light-driven ion transport. *J. Am. Chem. Soc.* **139**, 11726–11733 (2017).
19. Bhosale, S. et al. Photoproduction of proton gradients with π-stacked fluorophore scaffolds in lipid bilayers. *Science* **313**, 84–86 (2006).
20. Gust, D., Moore, T. A. & Moore, A. L. Mimicking photosynthetic solar energy transduction. *Acc. Chem. Res.* **34**, 40–48 (2001).
21. Lozada-Hidalgo, M. et al. Giant photoeffect in proton transport through graphene membranes. *Nat. Nanotechnol.* **13**, 300–303 (2018).
22. Graf, M. et al. Light-enhanced osmotic energy generation using MoS2 nanopores. *Joule* **3**, 1549–1564 (2019).
23. Jin, X. et al. Light-driven proton transmembrane transport enabled by biosemiconductor 2D membrane: a general peptide-induced WS2 band shifting strategy. *Biosens. Bioelectron.* **218**, 114741 (2022).
24. Liu, P. et al. Light-induced heat driving active ion transport based on 2D MXene nanofluids for enhancing osmotic energy conversion. *CCS Chem.* **3**, 1325–1335 (2021).
25. Wang, Z.-Y., Zhu, Y.-J., Chen, Y.-Q., Yu, H.-P. & Xiong, Z.-C. Flexible nanocomposite paper with superior fire retardance, mechanical properties and electrical insulation by engineering ultralong hydroxyapatite nanowires and aramid nanofibers. *Chem. Eng. J.* **444**, 136470 (2022).
26. Kwon, S. R. et al. Mechanically strong graphene/aramid nanofiber composite electrodes for structural energy and power. *ACS Nano* **11**, 6682–6690 (2017).
27. Tung, S.-O., Ho, S., Yang, M., Zhang, R. & Kotov, N. A. A dendrite-suppressing composite ion conductor from aramid nanofibres. *Nat. Commun.* **6**, 1–7 (2015).
28. Li, J., Tian, W., Yan, H., He, L. & Tuo, X. Preparation and performance of aramid nanofiber membrane for separator of lithium ion battery. *J. Appl. Polym. Sci.* **133**, 1–8 (2016).
29. Li, Y., Yuan, S., Zhou, C., Zhao, Y. & Van der Bruggen, B. A high flux organic solvent nanofiltration membrane from Kevlar aramid nanofibers with in situ incorporation of microspheres. *J. Mater. Chem. A* **6**, 22987–22997 (2018).
30. Ma, Z. et al. High-performance and rapid-response electrical heaters based on ultraflexible, heat-resistant, and mechanically strong aramid nanofiber/Ag nanowire nanocomposite papers. *ACS Nano* **13**, 7578–7590 (2019).

31. Mogg, L. et al. Atomically thin micas as proton-conducting membranes. *Nat. Nanotechnol.* **14**, 962–966 (2019).
32. Mogg, L. et al. Perfect proton selectivity in ion transport through two-dimensional crystals. *Nat. Commun.* **10**, 1–5 (2019).
33. Huynh, M. H. V. & Meyer, T. J. Proton-coupled electron transfer. *Chem. Rev.* **107**, 5004–5064 (2007).
34. Delley, B. An all-electron numerical method for solving the local density functional for polyatomic molecules. *J. Chem. Phys.* **92**, 508–517 (1990).
35. Perdew, J. P., Burke, K. & Ernzerhof, M. Generalized gradient approximation made simple. *Phys. Rev. Lett.* **77**, 3865 (1996).
36. Yang, M. et al. Dispersions of aramid nanofibers: a new nanoscale building block. *ACS Nano* **5**, 6945–6954 (2011).
37. Jain, A. & Vijayan, K. Kevlar 49 fibres: thermal expansion coefficients from high temperature X-ray data. *Curr. Sci. Bangalore* **78**, 331–335 (2000).
38. Penn, L. & Milanovich, F. Raman spectroscopy of Kevlar 49 fibre. *Polymer* **20**, 31–36 (1979).
39. Ji, H. et al. Fabrication of aramid-coated asymmetric PVDF membranes towards acidic and alkaline solutions concentration via direct contact membrane distillation. *Appl. Surf. Sci.* **562**, 150185 (2021).
40. Qin, R. et al. Nanofiber-reinforced clay-based 2D nanofluidics for highly efficient osmotic energy harvesting. *Nano Energy* **100**, 107526 (2022).
41. Zhao, W. et al. Osmotic energy generation with mechanically robust and oppositely charged cellulose nanocrystal intercalating G.O. membranes. *Nano Energy* **98**, 107291 (2022).
42. Sheng, N. et al. Enhanced salinity gradient energy harvesting with oppositely charged bacterial cellulose-based composite membranes. *Nano Energy* **101**, 107548 (2022).
43. Zhao, X. et al. Metal organic framework enhanced SPEEK/SPSF heterogeneous membrane for ion transport and energy conversion. *Nano Energy* **81**, 105657 (2021).
44. Chen, C. et al. Aramid nanofiber membranes for energy harvesting from proton gradients. *Adv. Funct. Mater.* **32**, 2102080 (2022).